Solar Physics
DOI: 10.1007/•••••-•••-•••-••••-•

The wings of Ca II H & K as photospheric diagnostics and the reliability of one-dimensional photosphere modeling

V.A. Sheminova

© Springer ••••

arXiv:1207.2020v1 [astro-ph.SR] 9 Jul 2012

Abstract

The extended wings of the Ca II H & K lines provide excellent diagnostics of the temperature stratification of the photosphere of the Sun and of other cool stars, thanks to their LTE opacities and source functions and their large span in formation height. The aim of this study is to calibrate the usage of the H & K wings in one-dimensional interpretation of spatially averaged spectra and in deriving per-pixel stratifications from resolved spectra. I use multi-dimensional simulations of solar convection to synthesize the H & K wings, derive one-dimensional models from these wings as if they were observed, and compare the resulting models to the actual simulation input. I find that spatially-averaged models constructed from the synthesized wings generally match the simulation averages well, except for the deepest layers of the photosphere where large thermal inhomogeneities and Planck-function nonlinearity gives large errors. The larger the inhomogeneity, the larger the latter. The presence of strong network fields increases such inhomogeneity. For quiet photospheric conditions the temperature excesses reach about 200 K. One-dimensional stratification fits of discrete structures such as granulation and small-scale magnetic concentrations give satisfactory results with errors that are primarily due to steep temperature gradients and abrupt changes of temperature with depth. I conclude that stratification modeling using the H & K wings is a useful technique for the interpretation of solar high-resolution observations.

Keywords: Models, photosphere - Granulation - Magnetic fields, photosphere - Spectral line, intensity and diagnostics

1. Introduction

The wings of the Ca II H & K lines at 3933 Å and 3968 Å span the solar photosphere in their formation which is relatively simple to interpret. They contain

Main Astronomical Observatory, National Academy of Sciences of Ukraine, 27 Akademika Zabolotnoho St., Kiev, 03680 Ukraine
email: shem@mao.kiev.ua

suitable blend-free windows to sample intensities as well as blends to sample Dopplershifts at different heights. The span of their height sampling is extraordinary wide. Ayres (1989) demonstrated that the opacity minimum at 4000 Å and the large short-wavelength Planck sensitivity to temperature make the H & K background continuum respond as deep as the H^- opacity minimum near 1.6 μm. The H & K cores are chromospheric at line center and sample the shock-ridden internetwork "clapotisphere" as H_{2V} and K_{2V} grains near line center (*e.g.,* Rutten, 1995). The extended wings sample all heights between these extremes, with clean single-peaked contribution functions because virtually all calcium resides in the Ca II ground state without sensitivity to Boltzmann and Saha population partitioning (Figure 6 of Leenaarts *et al.*, 2006b) and without sensitivity to NLTE population processes such as photon pumping or photon suction. The source functions of H & K also obey LTE–CRD until about 1 Å from line center (*e.g.,* Shine, Milkey, and Mihalas, 1975; Ayres, 1975; Uitenbroek, 1989). Owocki and Auer (1980) emphasized the closeness of its source function to LTE which results from the relatively high probability of wing-photon destruction by incoherent scattering into the thermal line core.

H & K wing modeling of solar and stellar photospheres was initiated during the 1970s at Boulder by J.L Linsky and collaborators, in particular T.R. Ayres (Ayres, Linsky, and Shine, 1974; Ayres and Linsky, 1975; Ayres, 1975, 1977). Later, Rouppe van der Voort (2002) used the technique on a sunspot penumbra. The original application to solar faculae by Shine and Linsky (1974) was followed by Sheminova, Rutten, and Rouppe van der Voort (2005, henceforth Paper I) to derive models of individual magnetic concentrations ("fluxtubes") from high-resolution H & K spectra. Ca II H wing modeling using an inversion SIR-code based on response functions was initiated by Beck *et al.* (2008). It serves to interpret large sets of spatially resolved line profiles in an automated manner. Recently, Henriques and Kiselman (2009) briefly described an application to high-resolution Ca II H filtergrams, including calibration using snapshots from numerical multi-dimensional simulations.

Even more recent are the new results of Uitenbroek and Criscuoli (2011) who demonstrate that the analysis of average spectra in terms of one-dimensional models is inherently unreliable because the inferred temperatures differ from the actual averaged temperatures. The average continuum of an atmosphere with temperature fluctuations is higher than the continuum of a one-dimensional atmosphere with the same average temperature stratification, due to the non-linearity of the Planck function with temperature. The interpretation of an average spectrum from a horizontally inhomogeneous atmosphere in terms of a one-dimensional model therefore leads to an overestimate of the average temperatures in the atmosphere. Since most of the information about solar and stellar atmospheres is obtained from unresolved spectra, it is important to assess this erroneous temperature excess in one-dimensional modeling of a mean spectra.

In the present paper the usage of the H & K wings as model-construction diagnostics is calibrated in an effort similar to the analysis of Henriques and Kiselman (2009) and Henriques, Kiselman, and van Noort (2010). The first goal of the paper is to estimate the reliability of one-dimensional modeling based on the Ca II H & K wings for characteristic fine structures of the solar

photosphere. The second goal is to quantify the temperature excesses produced by one-dimensional H & K wing modeling from unresolved spectra.

Three different numerical simulations are employed here:

- the 3D hydrodynamic (HD) simulation with the CO^{5}BOLD code described by Wedemeyer *et al.* (2004), henceforth called 3DHD;
- a 2D magnetohydrodynamic (MHD) simulation described by Gadun (2000) and Gadun *et al.* (2001), henceforth 2DMHD;
- a snapshot from a 3D magnetohydrodynamic simulation with the code of Stein and Nordlund (1998), henceforth 3DMHD. This snapshot was also used by Carlsson *et al.* (2004), Leenaarts *et al.* (2006a, 2006b), Tritschler and Uitenbroek (2006), Uitenbroek, Tritschler, and Rimmele (2007), and Henriques and Kiselman (2009).

For each snapshot I computed emergent absolute intensities throughout H & K and then used these as quasi-observed H & K spectra to derive a best-fit one-dimensional photosphere model. I do not consider any actual H & K observation in this paper, but compare these simulation-result fits to the actual stratifications in the original simulation snapshots and compare the different simulations as well.

In Section 2 I describe the simulation atmospheres, the spectral synthesis, and the procedure of one-dimensional model construction. The synthesized H & K spectra are presented in Section 3.1. The best-fit temperature stratifications of the average atmosphere inferred from spatially averaged synthetic H & K profiles and the evaluation of the temperature excesses are presented in Section 3.2. Best-fit temperature stratifications for granules, lanes and magnetic concentrations derived from spatially resolved H & K profiles are given in Section 3.3. Discussion and conclusions are given in Sections 4 and 5.

2. Method

2.1. Simulations

The 3DHD simulation reproduces photospheric granulation during a few hours of solar time. The simulation cubes measure $(x, y, z) = 5600 \times 5600 \times 3110$ km with an atmospheric extent of 1710 km in z above the zero "surface" level defined by mean optical depth $\log \tau_5 = 0$ at 5000 Å. The grid step is 40 km in x and y; the height sampling in z starts at 46 km at the base and is 12 km for $z > -270$ km. I used 55 simulation cubes at 60 s time steps to obtain averaged H & K profiles.

The 2DMHD simulation is representative of magnetogranulation with strong magnetic field, similar to network regions with fluxtube field strengths reaching 1.5–2 kG at the surface. The horizontal extent is about 4000 km, the vertical extent 735 km above and 1370 km below the zero "surface" level. The start-off initial magnetic field had bipolar geometry with loop connectivity and spatially averaged unsigned field strength 54 G, which increased with the simulation run time to a time-average of about 400 G at the surface. I used 52 snapshots at 30-s intervals.

The 3DMHD simulation snapshot measures $6000 \times 6000 \times 5000$ km with 2500 km atmosphere height above $\log \tau_5 = 0$. The grid step is 25 km horizontally, vertically 15 km in the upper layers and 35 km in the lower. The initial seed magnetic field was vertical and uniform with strength 250 G. The evolved snapshot contains magnetogranulation with a few fluxtubes in intergranular lanes with field strengths of about 1700 G. Weak horizontal magnetic fields occur in the granules.

2.2. Spectral synthesis

I modified the SPANSAT code described by Gadun and Sheminova (1988) for LTE spectral synthesis of the overlapping H & K lines including superimposed blends. It computes intensity spectra containing any selection of overlapping spectral lines from a given one-dimensional model atmosphere. The spectral line parameters were taken from the VALD database (Kupka *et al.*, 1999). The atomic parameters of the H & K Ca II lines are the same in Paper I, with calcium abundance $A_{\rm Ca} = 6.38$ and $\log gf = 0.134$ for Ca II K, -0.18 for Ca II H.

Micro- and macroturbulent velocities have small effect on the extended H & K wings. I did not apply micro and macroturbulence in the line synthesis from the simulations since their velocity field is given with the data cubes. In the subsequent fitting procedure I applied microturbulence in the line profile synthesis following Gurtovenko and Sheminova (1986) with the total velocity amplitude $V_t = 1.6$ km s^{-1} determined as $V_t^2 = V_{\rm mic}^2 + V_{\rm mac}^2$. This approach simplifies the H & K profile calculation without loss of accuracy.

Collisional damping by neutral hydrogen atoms was formerly a major uncertainty which has been resolved by the code of Barklem and O'Mara (1998) based on quantum-mechanical estimation. I used it here.

In Paper I, which compared observed and computed H & K wing profiles, we had to cope with the "line haze" of unresolved weak lines in this part of the spectrum, for which we applied ad-hoc scaling factors

$$f = 1 + c\,(N_{\rm H}/N_{\rm H^-}) \tag{1}$$

to the computed continuum opacity. The constants c were determined from comparing synthetic far wings computed for disk center to the observed far wings. Since the present study does not involve actual observations this contribution is neglected here.

In addition, no profile comparisons are made within 1 Å from line center to avoid effects from coherent scattering. The effects of magnetic fields on H & K wing formation are neglected. All 2912 overlapping lines of neutral and single ionized atoms in the VALD list are entered as blends. In between these, I selected 28 relatively blend-free wing windows as the sampling wavelengths that define what I call "H & K profile" here. Such profiles were synthesized for all columns of all simulation snapshots. Then the average line profile was computed by averaging all these individual profiles per simulation.

The major assumption in this computation is one-dimensional LTE radiative transfer along columns. Owocki and Auer (1980) have shown that the unresolved

Mg k and Ca K wings are not sensitive to the horizontal transfer effects and may be used as potentially good atmospheric diagnostics in the multi-component (1.5D) sense without significant errors. More recently, Leenaarts *et al.* (2010) have demonstrated that 3D radiative transfer effects only become noticeable at much larger height, as for example in the 3D evaluation of Na D_1 formation.

2.3. One-dimensional model construction

As in the classical H & K wing modeling I apply trial-and-error fitting of the synthetic line profiles by changing the temperature stratification with height in the atmosphere as for a plane-parallel atmosphere.

The initial start-off model gives the temperature $T(h)$ and gas pressure $P_g(h)$ stratifications depending on the geometric height h (positive outwards). For the mean atmosphere modeling and for fitting granular fine structure I chose the HSRA-SP-M model as the start-off stratification. This is the HSRA model of Gingerich *et al.* (1971) modified by Spruit (1974) and again modified in Paper I. Note that HSRA-SP-M contains very deep layers of the atmosphere. The PLANEW reference model for a strong magnetic fluxtube by Solanki and Brigljevic (1992) was chosen as the initial model for the modeling of small-scale magnetic elements.

In each iteration the temperature stratification was changed manually at 14–17 geometrical height samples. Their distribution with height is irregular and was selected depending on the temperature gradients for the simulated object. The initial set of the height points (in kilometers) for the start-off HSRA-SP-M was the following: 864 (-6.7), 300, 200, 150, 100, 75, 50, 25, 0, -25, -50, -100, -150, -300, -409 (3.5). For PLANEW as start-off the set was 659 (-6.2), 300, 200, 150, 100, 75, 50, 25, 0, -25, -50, -100, -150, -300, -306 (0.8). The highest and deepest optical depths are given between brackets, in logarithmic units. The temperature at other heights was computed by spline interpolation. The resulting best-fit stratifications extend down to the deepest geometrical depth. Since the deepest optical depth depends on the specific opacity $\kappa_\lambda(T,\ P_g)$ it depends on the simulated feature.

At each temperature modification a new gas pressure stratification was computed assuming vertical hydrostatic equilibrium. The equation of hydrostatic equilibrium can be integrated in many ways. I used:

$$P_g(h) = P_0\ \exp\ [-\frac{g}{R}\int_{h_0}^{h}\frac{\mu_0(h')}{T(h')}\,\mathrm{d}h'], \tag{2}$$

where g is the gravitational acceleration, R the gas constant, $\mu_0(h)$ the variable mean molecular weight taking into account the partial ionization of the various chemical elements. P_0 is defined as the gas pressure at the bottom of the atmosphere (h_0) accounting for the adopted chemical composition. The SPANSAT code calculates the electron pressure P_e as a function of depth from $P_g(h)$ and the equation of state for ideal gas including LTE evaluation of the ionization equilibrium for all pertinent elements according to the scheme by Mihalas (1967) with minor changes. In this work the chemical composition corresponds to data

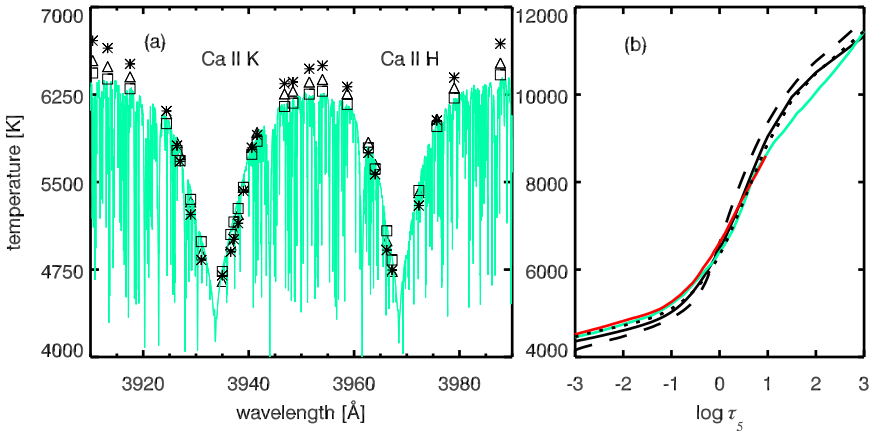


Figure 1. (a) Mean H & K profiles synthesized from 3DHD (triangles), 2DMHD (asterisks), and 3DMHD (squares). The green observed profile with numerous blends is copied from the the disk-center Brault-Neckel atlas by Neckel (1999). The intensity units were converted into brightness temperature. (b) Mean temperature stratification for the 3DHD (solid), 2DMHD (dashed), and 3DMHD (dotted) simulations. The spatial averaging was done over surfaces of equal optical depth τ_5. The temperature stratification of the quiet photosphere derived from unresolved observed spectra HSRA-SP-M (Paper 1) and SRPM-305 (Fontenla, Balasubramaniam, and Harder, 2007) is presented by green and red curves, respectively.

from the paper of Fontenla, Balasubramaniam, and Harder (2007). It is given as a table of abundance values for 104 chemical elements and it does not change during the fitting procedure. Thus, the free atmospheric parameters are $(14-17)\times T$, P_0 in our one-dimensional modeling.

As in other inversion methods each subsequent iteration minimizes the sum of the squared differences between the original and synthetic H & K profiles for 28 wavelength points. The procedure of the minimization is complex due to the nonlinear dependence of the emergent intensity on the atmospheric parameters that control the radiative transfer. To succeed one must gain experience in how the intensity of the H & K profile responds to temperature changes of specific layers of the photosphere.

Such fitting was done for the spatial average of each simulation and for single simulation pixels for which the modeling resolved specific fine structure (granule, intergranular lane, small-scale magnetic element).

3. Results

3.1. Synthesized spectra

Figure 1a shows the averaged H & K profiles synthesized from all columns of the 3DHD, 2DMHD, and 3DMHD simulations. For the first two simulations the profile averaging is done over all columns of all snapshots, i.e., over both surface and time. In the third case the averaging is done over all columns of the single snapshot, i.e., only over surface. For comparison Figure 1a also shows

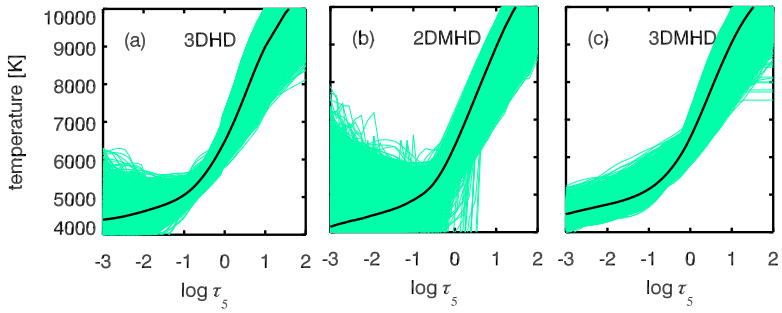


Figure 2. Temperature against optical depth for all columns of a snapshot of the 3DHD and 3DMHD simulations and for all columns of the time series of 2DMHD. The solid curve is the mean.

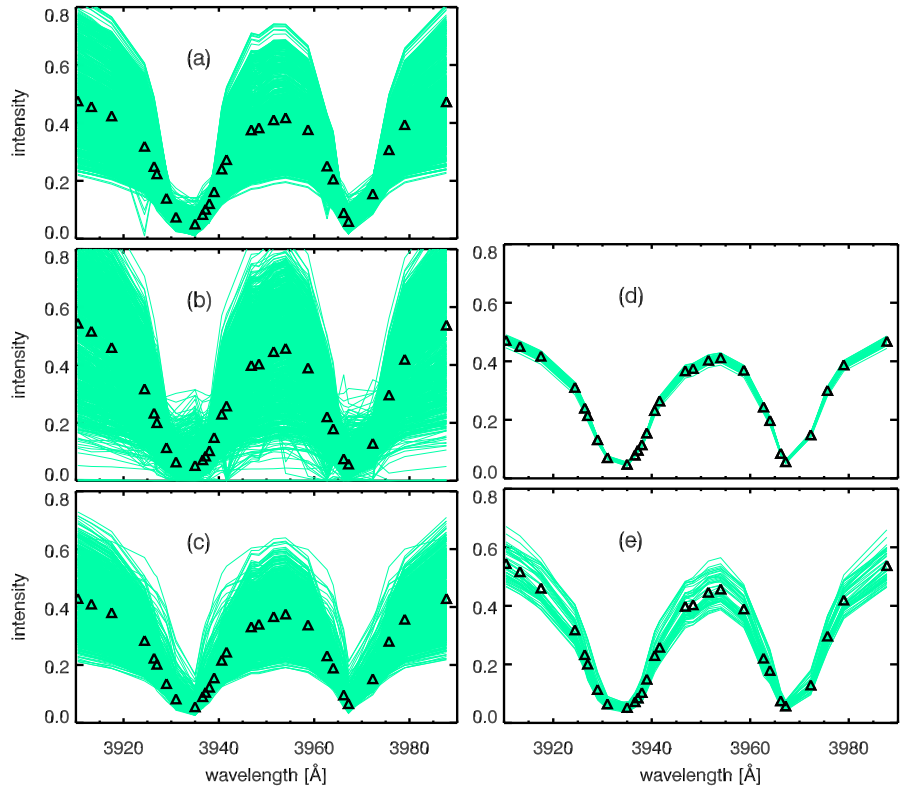


Figure 3. Synthetic H & K profiles for all columns of all snapshots of 3DHD (a), 2DMHD (b), and a snapshot of 3DMHD (c). Temporal variations between profiles from all snapshots of the 3DHD (d) and 2DMHD (e) simulations. The symbols specify the mean value. In this and other figures the absolute intensity is given in watt $\mathrm{cm}^{-2}\,\mathrm{ster}^{-1}\,\mathrm{\AA}^{-1}$.

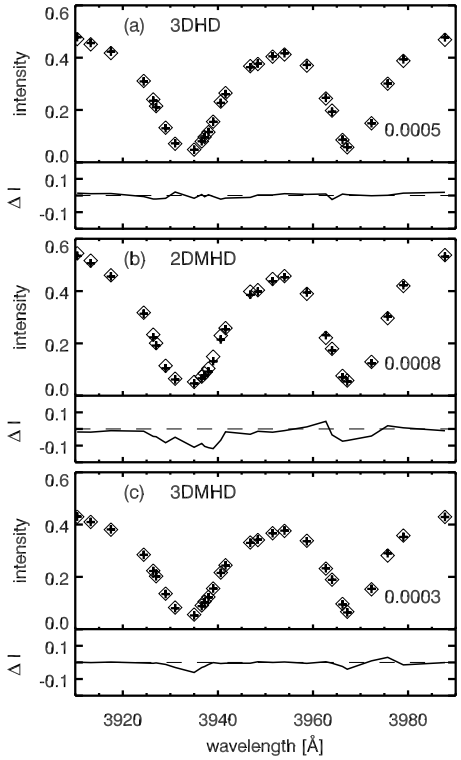


Figure 4. Best-fit H & K profiles (crosses) compared to the temporal and spatial averages of the synthetic profiles (rhombuses) from the 3DHD (a), 2DMHD (b), and 3DMHD (c) simulations. The lower panels of each subfigure show residuals $\Delta I = (I - I_{\rm original})/I_{\rm original}$, i.e., the differences between the synthetic and original profiles in the relative units. The standard deviation $\sigma(I - I_{\rm original})$ are indicated in the lower-right corner of each subfigure.

observed H & K profiles from the disk-center atlas taken by J.W. Brault with the NSO Fourier Transform Spectrometer and made available by Neckel (1999) after calibration to the absolute intensities of Neckel and Labs (1984). The three synthesized profiles agree reasonably with the atlas spectrum. However, the outer wings of the 2DMHD profile reach appreciably larger intensities than the other profiles.

Figure 1b shows the average temperature stratification for the three simulations, *i.e.,* averaging both spatially and temporally for 3DHD and 2DMHD, spatially only 3DMHD. The spatial average is evaluated over surfaces with equal continuum optical depth τ_5 as in Uitenbroek and Criscuoli (2011). They showed that such equal-τ_5 averaging represents emergent intensities better than averaging over planes of equal geometrical depth.

As may be seen from Figure 1b, in the deep layers below $\log \tau_5 = 0$ the mean gradient is smallest for 3DMHD and largest for 2DMHD. A steeper temperature gradient in deep layers produces larger emergent intensity in the outer wings. For comparison Figure 1b adds the one-dimensional H & K line-fitting HSRA-SP-M model (Paper 1) used here to start the fitting procedure and the standard

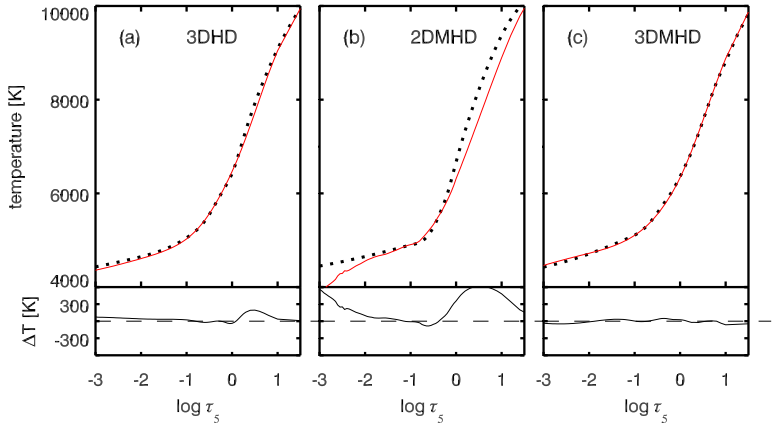


Figure 5. Temperature stratifications of the best-fit models (dotted) compared to the equal-τ_5 averages of the simulations (red curve). The lower panels present the residual temperatures $\Delta T = T_{\rm best-fit} - T_{\rm original}$.

one-dimensional continuum-fitting SRPM-305 model of Fontenla, Balasubramaniam, and Harder (2007). Their temperature stratifications have lower gradients compared with the simulation averages.

Figure 2 demonstrates the spread around the mean temperature stratification for each simulation. The spread caused by thermal inhomogeneities differs substantially between the three simulations. In high layers they are largest for 2DMHD and remarkably small for 3DMHD; in deep layers they are more similar.

Figures 3a,b,c show the spatial spread in the H & K intensities computed from the simulations, using all snapshots. In each case, the spread increases towards the wings with larger temperature spread at larger formation depth.

Figures 3d,e show the temporal variations between snapshots for 3DHD and 2DMHD. The variability is largest for 2DMHD, probably reflecting growth in inhomogeneity because the magnetic field strength and oscillations increase with time.

3.2. Best-fit stratifications from spatially averaged synthetic profiles

This section presents best-fit results using the averaged H & K profiles. Figure 4 shows the best-fit synthesized H & K profiles with the spatially averaged H & K profiles from all columns of 3DHD, 2DMHD, and 3DMHD, respectively. For each fitted profile the standard deviation is

$$\sigma(I - I_{\rm original}) = \sqrt{\frac{1}{n}\sum_{i=1}^{n}(I(\lambda_i) - I_{\rm original}(\lambda_i))^2}, \qquad (3)$$

where the wavelength index $i = 1, ..., n$ sample the wavelengths at which spectrum is known, $n = 28$, $I(\lambda)$ is the intensity synthesized from the one-dimensional model, and $I_{\rm original}(\lambda)$ is the average intensity over the simulation. The largest values is $\sigma = 0.0008$ for 2DMHD which has the largest temperature spread

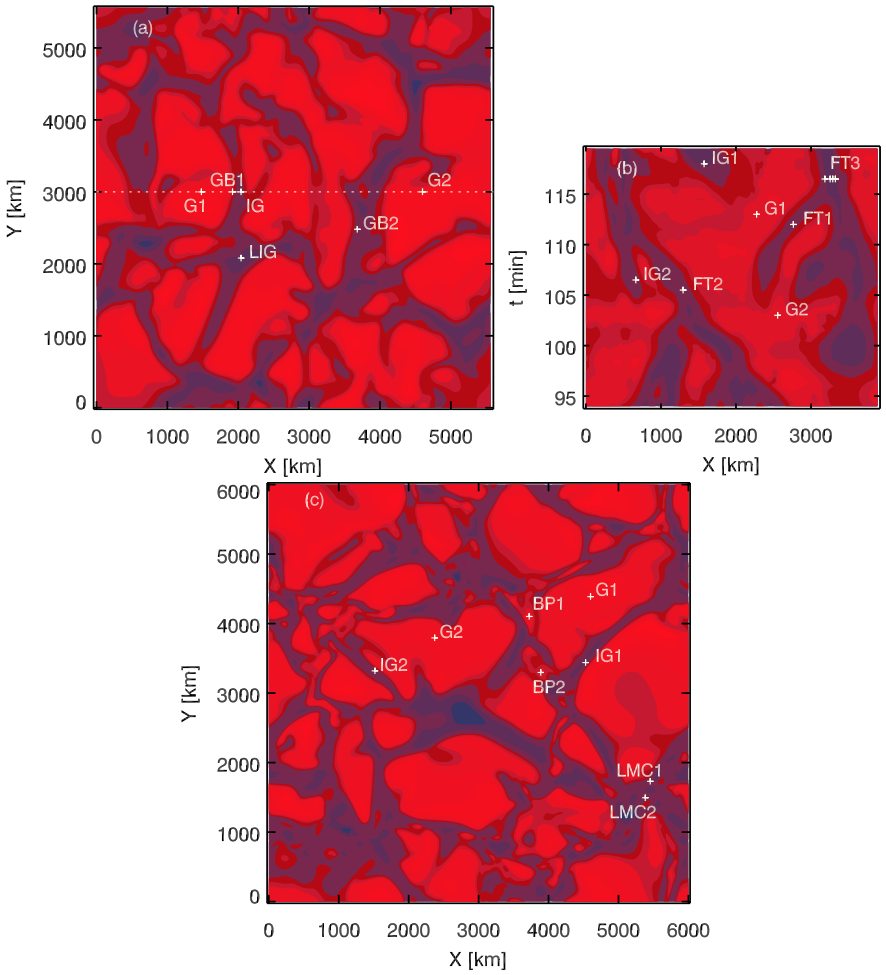


Figure 6. Continuous intensity images at $\lambda = 3910$ Å for a 3DHD snapshot (a), the time series of 2DMHD (b), and a 3DMHD snapshot (c). The locations selected for feature modeling are marked with crosses and identifiers with designations: G1 and G2 for granule centers, GB1 and GB2 for granule borders, IG, IG1 and IG2 for intergranular lanes, LIG for a large intergranular lane, BP1 and BP2 for bright points, LMC1 and LMC2 for large magnetic concentrations, FT1 and FT2 for centers of thin and moderate fluxtubes. FT3 is a strong fluxtube. A cross in its center is called FT3-0 in the text; crosses to the left of center in the direction of the fluxtube periphery are called FT3-1, FT3-3, and FT3-5. The dotted line shows the selection of columns for the calculation of intensity and temperature fluctuations presented in Figure 14.

and gradient. In addition, the lower panels show residuals ΔI for quick assessment of the fit quality. These are normalized to $I_{\rm original}$ per wavelength as $\Delta I = (I - I_{\rm original})/I_{\rm original}$.

Figure 5 compares the corresponding best-fit temperature stratifications (dotted) to the simulation averages (solid red). The best agreement between the best-fit stratifications and the simulation averages occurs over $\log \tau_5 = [0, -2]$. Higher up the best-fit temperatures lie above the averages, especially for 2DMHD

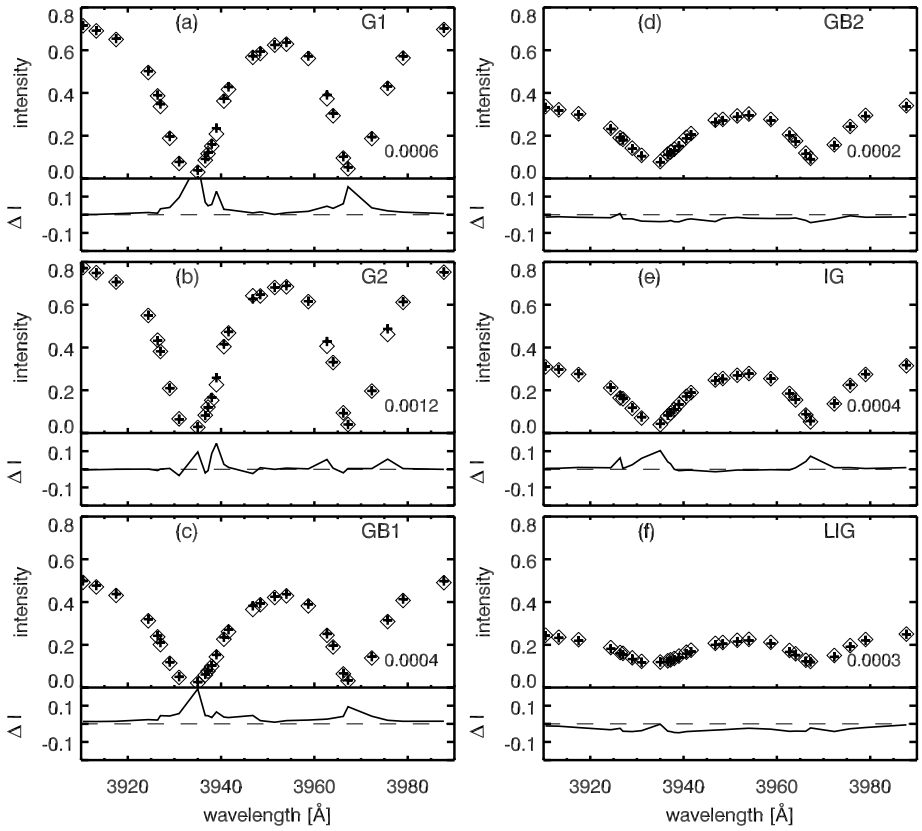


Figure 7. Best-fit H & K profiles (crosses) compared to synthetic profiles from single 3DHD columns (rhombuses) for granule center (G1, G2), granule borders (GB1, GB2), an intergranular lane (IG), and a large intergranular lane (LIG). The symbol and number coding are the same as in Figure 4.

due to the larger thermal inhomogeneity of 2DMHD (Figure 2b). Near $\log \tau_5 \approx 0.5$ the best-fit stratifications lie above the averages for all three simulations. Figure 5 also shows that the temperature residual $\Delta T = T_{\rm best-fit} - T_{\rm original}$ reaches a maximum of about 600 K for the 2DMHD stratifications, probably due to the growth of magnetic inhomogeneity.

3.3. Best-fit temperature stratification from spatially resolved H & K profiles

In this section a few columns corresponding to specific fine-structure features (granule center, granule border, intergranular lane, individual magnetic concentration) are selected for best-fit modeling.

Figure 6 shows continuum images at $\lambda = 3910$ Å constructed from the three simulations with labels at the selected locations. The small-scale magnetic elements in 2DMHD were selected with the help of vertical cross sections though the computational domain. In the 3DMHD simulation, they were selected according to the data of Carlsson *et al.* (2004).

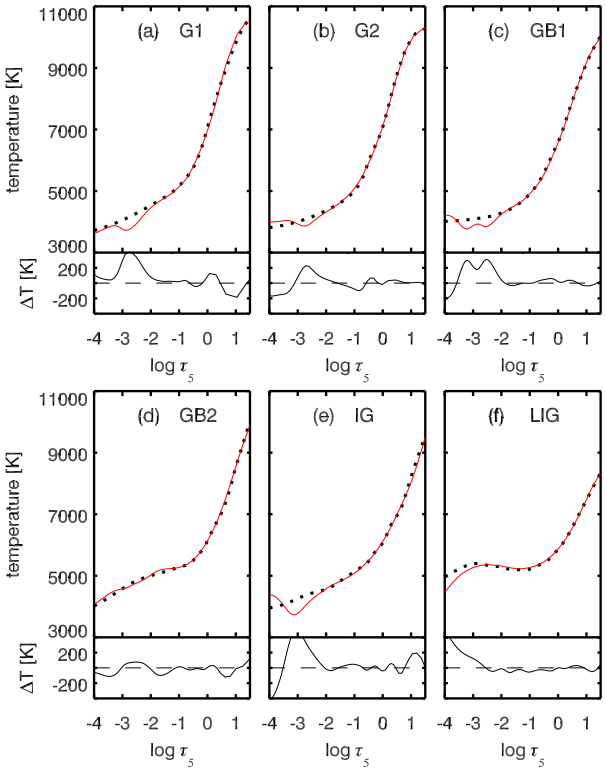


Figure 8. Best-fit temperature stratifications (dotted curves) derived from single 3DHD columns for the same locations as in Figure 7. Symbol and curve coding as in Figure 5.

Figures 7, 9, and 11 show the best-fit results of the corresponding resolved emergent profiles. The best-fit synthesized H & K profiles (crosses) and the profiles synthesized from the individual columns of the numerical simulation (rhombuses) are in close agreement. The statistic estimations $\sigma(I - I_{\rm original})$ in the lower-left corners and the residuals (in relative units) in the lower panels show the fit quality.

Note the diversity between profiles from different types of granular structure. The steep wing slope becomes more gentle from a granule center to its borders and to a lane (Figure 7). The profile changes between the centre and periphery of strong fluxtubes are seen in Figures 9g–j. The profiles from the bright points (Figures 11e,f) are the narrowest.

Figures 8, 10, 12 show the best-fit temperature stratifications (dotted) and the corresponding original 3DHD, 2DMHD, 3DMHD columns (red). In general, the agreement is satisfactory. Some differences occur at temperature irregularities in the original stratifications (e.g., Figures 10a,b,f,e). As is seen from these figures, the temperature residuals ΔT are associated with the irregularities except for the large ΔT (200–400 K) at $\log \tau_5 = 0$ in Figure 10a,b.

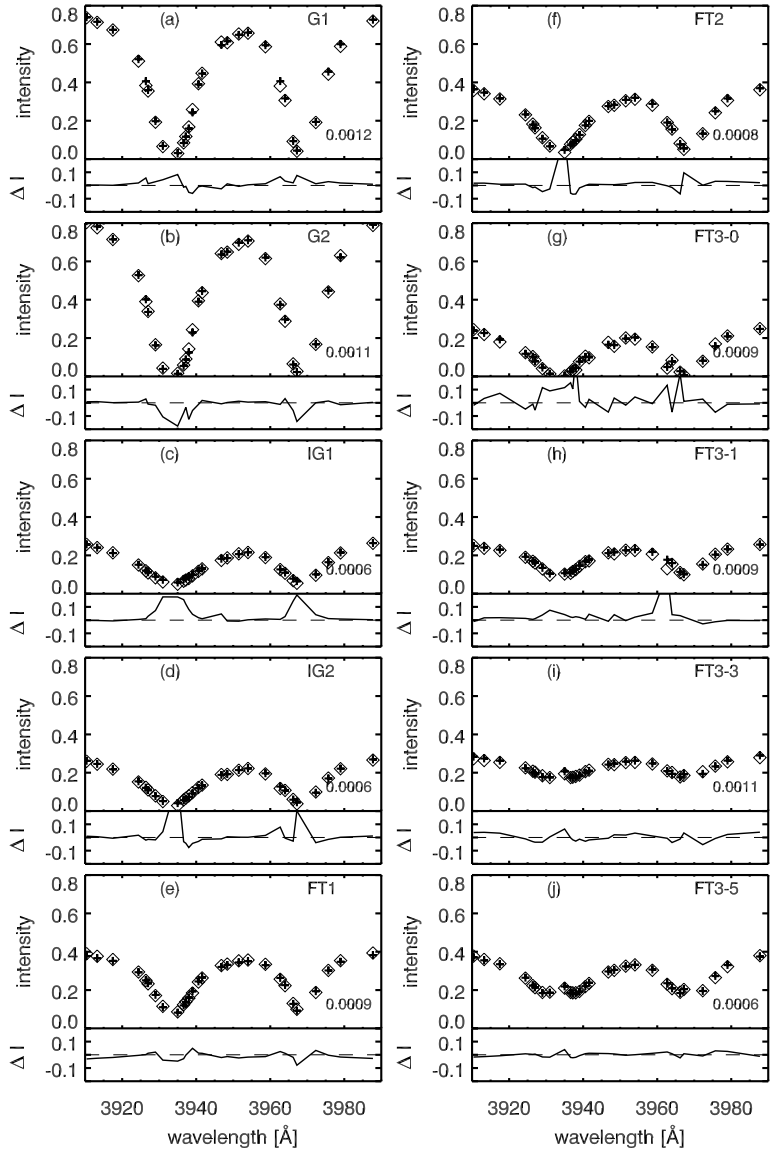


Figure 9. Best-fit H & K profiles from 2DMHD for granule center (G1, G2), intergranular lanes (IG1, IG2), thin fluxtube (FT1), moderate fluxtube (FT2), and four locations in the strong fluxtube (FT3-0, FT3-1, FT3-3, and FT3-5). Symbol and curve coding as in Figure 4.

4. Discussion

The discrepancies between the quiet-Sun atlas spectrum and the averaged profile from the 3DHD simulation without magnetic fields (Figure 1a) may have two causes. The first is the neglect of the "line haze" which affects the atlas profile but is not accounted for in the simulated profiles. Figure 13 shows that inclusion of a

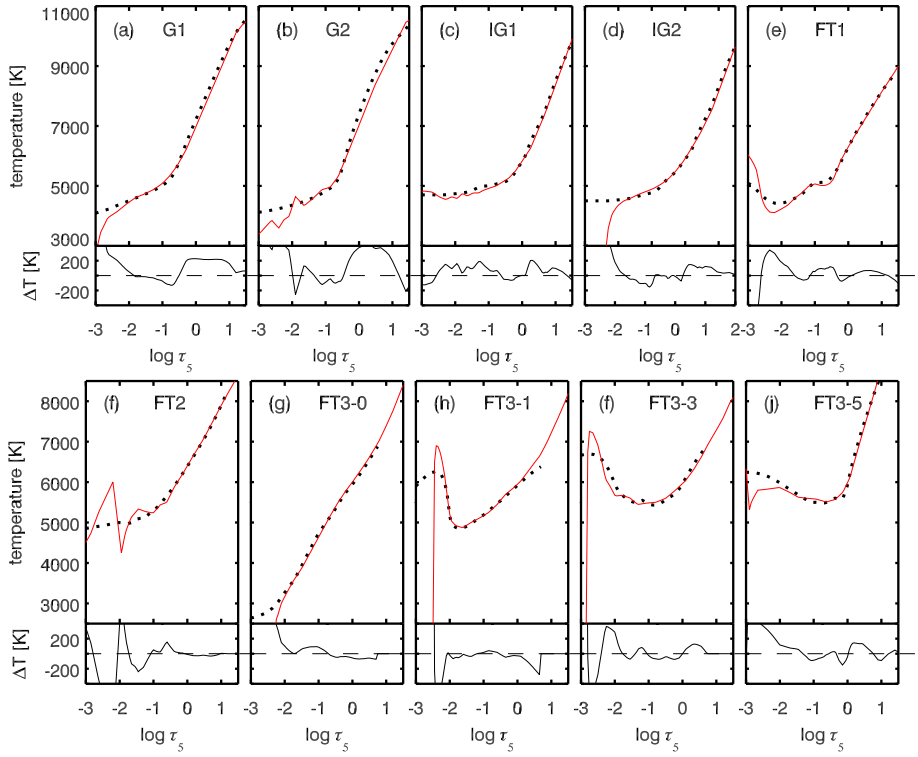


Figure 10. Best-fit temperature stratifications from 2DMHD. Symbol and curve coding as in Figure 5.

"line haze" in the H & K profile synthesis can significantly decrease the intensity in the H & K wings. Unfortunately, choosing an appropriate height-dependent fudge factor is not trivial. The second reason is that the temperature fluctuations in the simulation may not reproduce those in the real Sun. Evaluation of the simulation correctness is beyond this paper.

The differences between the averaged profiles derived from the three simulations (Figure 1a) can be due to the difference in the temperature inhomogeneities, gradients, and magnetic field density ($<|B|>$). Figure 2b shows the largest temperature spread for 2DMHD which represents magnetogranulation with $<|B|> = 400$ G in strong network. The large temperature spread in the higher layers of the 2DMHD increases the inner-wing intensities. It is caused by the presence of many magnetic network elements. Figure 2b shows many sharp temperature drops and rises caused by the strongest magnetic fields within the fluxtubes and at their hot walls at the peripheries. This follows from the analysis of vertical cross sections through the computational domain in the 2DMHD sequence. An example is Figure 10 of Paper 1. The temperature gradient of 2DMHD is also the steepest one in Figure 1b.

The temperature fluctuations observed as granulation of the solar surface are created by penetrating convective flows. The thermodynamic properties of the granulation are described by Stein and Nordlund (1998) in detail. The temper-

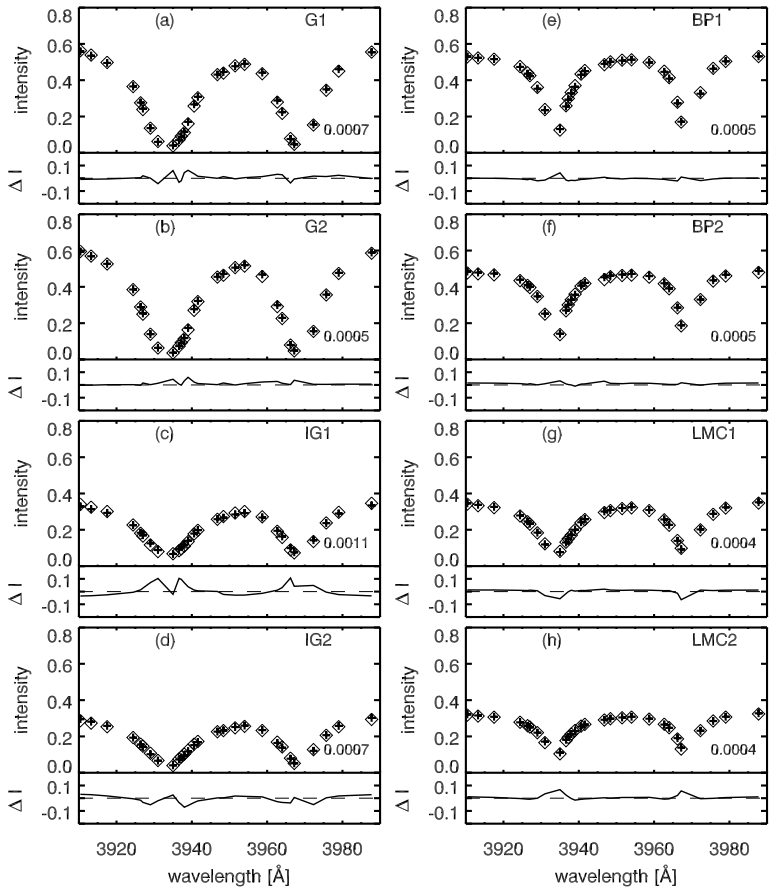


Figure 11. Best-fit H & K profiles from 3DMHD for granule center (G1, G2), intergranular lanes (IG1, IG2), bright points (BP1, BP2), and large magnetic concentrations (LMC1, LMC2). Symbol and curve coding as in Figure 4.

ature and density of the plasma near the surface have approximately bimodal distributions. The intergranular lanes have low temperature, very low ionization, and high density. The granules have high temperature, high ionization, and low density. The granules occupy larger area than the lanes. Below the surface they occupy $\approx \frac{2}{3}$ of the total area. Here the radiative cooling proceeds very rapidly. Since the H^- opacity is dominant and very temperature sensitive ($\approx T^{10}$), the steepest vertical temperature gradient results near the surface in the granules.

The presence of magnetic field in a simulation also affects the granulation. Gadun (2000) showed that the granulation pattern differs for magnetogranulation: the granules are larger and the shearing instability is stronger in the absence of magnetic fields. The field has a stabilizing effect – the granules are smaller and there are no pronounced horizontal shears. The distribution of granules in magnetogranulation differs from the nonmagnetic granulation by a greater contribution of bright features, which are associated with bright points in flux tubes. Therefore the granular contribution to the emergent intensity can also

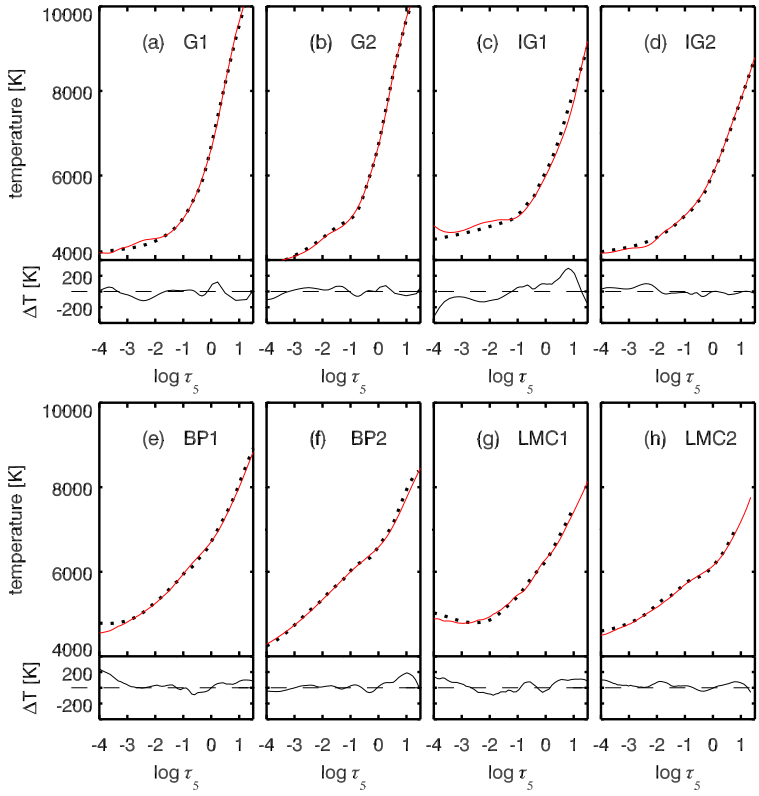


Figure 12. Best-fit temperature stratifications from 3DMHD. Symbol and curve coding as in Figure 5.

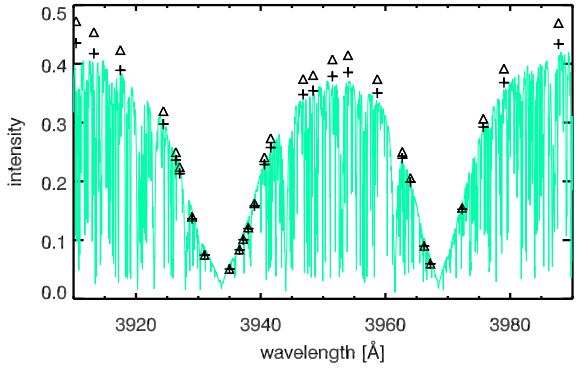


Figure 13. Average H & K profiles computed without (triangles) and with (pluses) line-haze fudge factor of $c = 0.14$ in Eq. (1) for the 3DHD simulation. The green observed profile from the Brault-Neckel atlas.

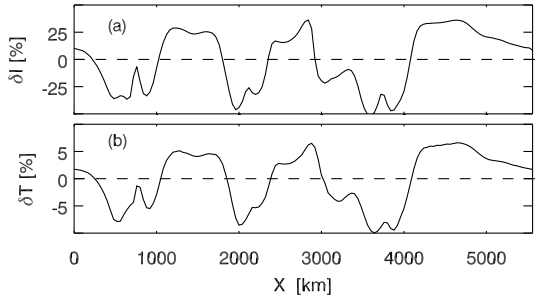


Figure 14. Fluctuations of the emergent intensity (δI) in the far wing of the Ca II H line at $\lambda = 3910$ Å. The temperature fluctuations (δT) at the optical depth equal to unity inferred from a set of columns are signaled by the dotted line in a 3DHD snapshot (Figure 6a).

differ between field-free granulation and magnetogranulation depending on the magnetic field density.

In spatial averaging the temperature fluctuations have different effect on the temperature average and on the average emergent intensity, due to the nonlinear dependence of the Planck function on temperature (Uitenbroek and Criscuoli, 2011). Indeed, Figure 14 shows intensity and temperature fluctuations ($\delta I = (I - <I>)/<I>$ and $\delta T = (T - <T>)/<T>$) computed for a set columns through of a 3DHD snapshot (marked by a dotted line in the Figure 6a). Here $<T>$ is the mean temperature along the selected cut in this snapshot at optical depth equal to unity. $<I>$ is the emergent intensity in the far wing of the Ca II H line at $\lambda = 3910$ Å averaged along the selected cut. The intensity fluctuations differ significantly in percentage from the temperature fluctuations. The relatively small temperature fluctuations $\delta T = 5\%$ produce large intensity fluctuations $\delta I = 50\%$. The intensity contributions to the average profile from the columns located within the granules are larger than from the columns located in intergranular lanes. This means that the averaged surface intensity from a simulation, i.e., averaged over the columns of a multi-dimensional simulation, is larger than the average intensity calculated from the averaged simulation.

Figure 15 shows the excess intensity between such averaged H & K profiles and the profiles synthesized from each spatially-averaged simulation. The continuum excess in relative units at $\lambda = 3910$ Å amounts to 7% for 3DHD, 38% for 2DMHD, and 7% for 3DMHD. The intensity excess in the far wings is close to the continuum excess. Figure 5 demonstrates that the best-fit procedure leads to overestimation of the temperature at continuum formation heights. The maximum temperature excesses are 194 K (3DHD), 619 K (2DMHD), and 48 K (3DMHD). The larger the temperature inhomogeneities, the higher is the best-fit continuum and the larger the temperature excess of the best-fit average temperature stratification. Thus, in the deepest layers of the quiet photosphere the one-dimensional modeling of the mean atmosphere give overestimation of about 200 K, whereas in the strong network regions the overestimation can reach 600 K.

The best-fit stratifications for the discrete fine-structure elements derived from the synthetic H & K spectra in Figures 8, 10, 12 recover the original temperature

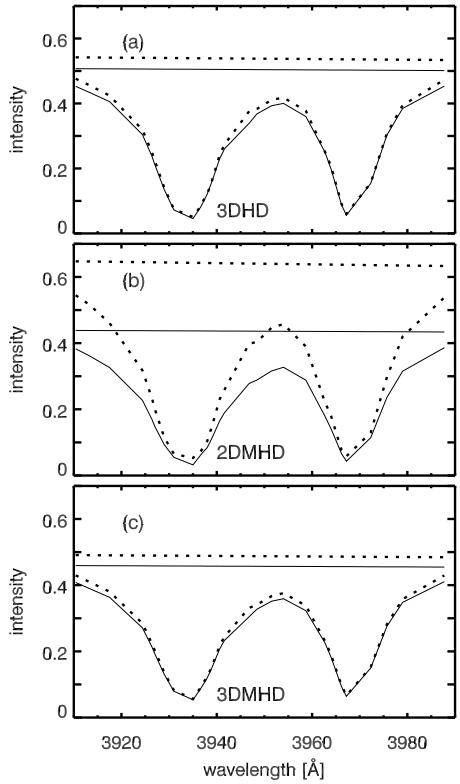


Figure 15. Averaged line profiles synthesized from the 3DHD, 2DMHD, 3DMHD simulations (dotted curves) and the profiles synthesized from their average temperature stratifications (solid), as well as the corresponding continua.

stratifications satisfactorily. Notice that the fitting procedure applied here recovers successfully both a temperature stratification which decreases monotonically with height and stratifications with a mild or steep temperature rise in higher layers (Figures 8f, 10e,h,f,j, 8d, 10c, 12c,e,f,g,h). The question arises whether it is possible to identify a temperature rise from the H & K profiles alone. Figures 7, 9, 11 show that H & K profiles calculated for temperature-rise stratifications have higher intensity near the line core the for a stratification with decreasing temperature. Probably, this diagnostic can be employed indicator of an atmospheric temperature rise.

In Figures 8, 10, 12 the temperature residuals $\Delta T = T_{\rm best-fit} - T_{\rm original}$ reflect the intrinsic uncertainties of the method used. For example, Figure 10b shows large (about 400 K) deviations from the original models at $\log \tau_5 = 0$, i.e., large deficiencies of the method. Tests showed that adding radiation pressure, magnetic pressure, and turbulent pressure in Eq. (2) makes no significant difference. Since the chemical composition is the same for the profile synthesis and the best-fit modeling it does not affect the results. The real cause for such deviations may be a effect of thermal irregularities in the vertical direction on the best-fit stratification. The effect is tested in Figure 16. The smooth temperature

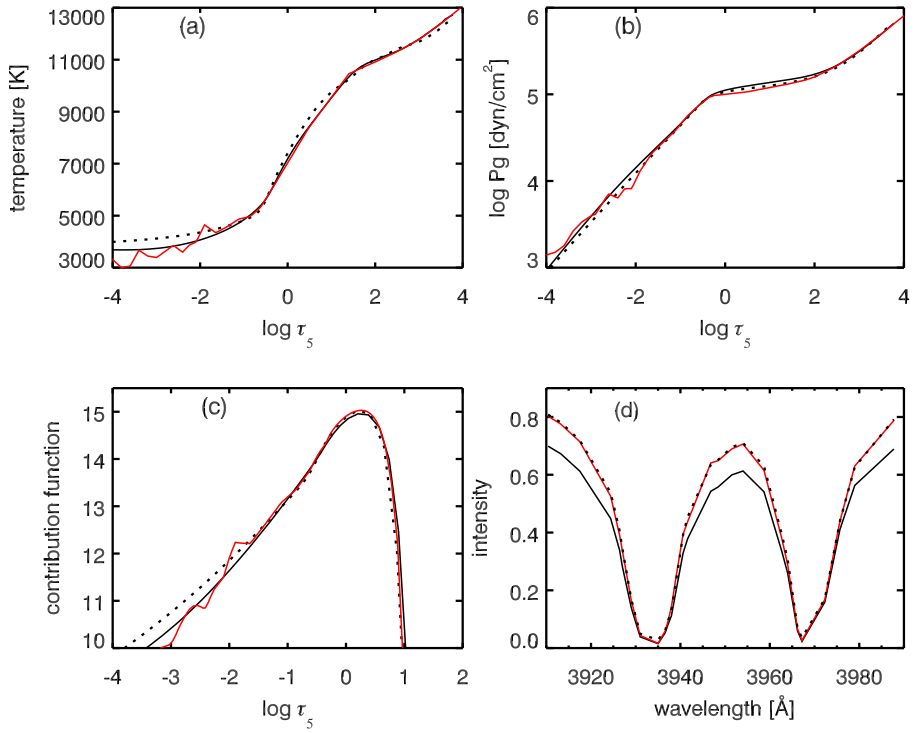


Figure 16. Temperature (a) and gas pressure (b) stratifications for a granule (Figure 10b) as well as contribution functions (c) to the emergent intensity at $\lambda = 3910$ Å and line profiles (d): original (red curves), smoothed (black), and best fit (dotted). Contribution functions are given in logarithmic units.

stratification (black curve) differs from the original (red curve) at locations where there are sudden temperature changes with depth. Such thermal irregularities are not recovered by the method used. In Figure 16b the gas pressure $P_g(h)$ (black) derived from the smooth $T(h)$ with Eq. (2) has excesses compared to the original one (red) at the locations corresponding to sharp temperature gradients. The synthesized H & K profile (black) with the smooth $T(h)$ therefore does not match the original profile (red) in Figure 16d. The corresponding black contribution function for the intensity at $\lambda = 3910$ Å (Figure 16c) is slightly lower than the red one due to increase of the damping ($\gamma_{\rm wdw} \approx P_g$) and the line opacity $\kappa(T, P_g)$. It causes lower emergent intensity in the far wings. To obtain a best line-profile fit the temperature increases and the pressure decreases (see dotted curves). Therefore the best-fit temperature (dotted curve) demonstrates the excess about 400 K in Figure 16a.

Complex non-monotonic temperature stratification such as in Figure 10d,e,f also cannot be reproduced by the manual fitting procedure used here. In addition, in the manual fitting the initial $T(h)$ and especially $P_g(h)$ stratifications in the deepest layers must be as close as possible to the real ones. So, for example, in the case of magnetic elements it is not possible to obtain best-fit profiles with the HSRA-SP-M model as initial guess, whereas the PLANEW fluxtube

model gives good results. These are shortcomings of the manual technique which diminish when using automatic inversion codes (e.g., Bellot Rubio, Ruiz Cobo, and Collados, 1997; Frutiger *et al.*, 2000) that search for a best fit by means of a Marquardt nonlinear least-squares algorithm. They can locate the minimum of the merit function more precisely than a manual procedure. The retrieved temperature stratification by the automatic inversion codes is largely independent of the choice of the initial guess atmosphere. Note, it is a limitation for the manual technique, but not for the H & K wings photospheric diagnostics. Therefore, it is desirable to develop such inversion codes for fitting H & K profiles.

5. Conclusion

The extended wings of Ca II H & K supply relatively easy diagnostics to extract quantities that describe vertical stratification of the solar photosphere. I have calibrated such one-dimensional modeling using three numerical simulations of solar fine structure, containing granular convection with different amounts of magnetic flux. I obtained best-fit temperature stratifications from synthetic H & K wing profiles computed from these simulations. Quantitative evaluation permits the following conclusions.

The different effect of thermal inhomogeneities on the average temperature stratification and on the average emergent intensity due to the non-linear Planck function sensitivity leads to overestimation of temperatures derived in such one-dimensional modeling. For quiet-Sun conditions this overestimation reaches about 200 K in the continuum formation layers. The larger the inhomogeneity, the larger the excess. The largest overestimation occurs for one-dimensional modeling at field strengths similar to the 2DMHD simulation, and can be as large as 600 K for strong magnetic fields when average profiles are analyzed. Such temperature overestimation may also occur in the upper photosphere due to large temperature contrasts between hot fluxtube walls and cool fluxtube insides.

The H & K wing diagnostics provide better recovery of the actual temperature stratifications within discrete fine structure elements such as a granule center, an intergranular lane, a bright point, a fluxtube, a large magnetic concentration. Here errors occur only where there are sharp vertical gradients and non-smooth irregularities in the original temperature stratification.

The range of effective formation of the emergent intensity in the wings of Ca II H & K extends from $\log \tau_5 = -2$ to 0.2. Beyond this depth range the reliability of the H & K wing diagnostics is less.

In conclusion, one-dimensional H & K wing modeling using high-resolution data is a reliable technique to construct best-fit models for small-scale features in the solar photosphere.

Acknowledgements I am much indebted to Rob Rutten for suggesting this analysis and for extensive improvement of the text, to Sven Wedemeyer-Böhm, Robert Stein, and Åke Nordlund for the use of the 3DHD and 3DMHD simulations, and to Jorrit Leenaarts, Mats Carlsson and Rob Rutten for providing

these. I am grateful to an anonymous referee for the many helpful comments and important suggestions to improve significantly the presentation of this paper.

References

Ayres, T.R.: 1975, Semiempirical upper photosphere models - The sun /G2 V/ and Procyon /F5 IV-V/. *ApJ* **201**, 799 – 815. doi:10.1086/153946.

Ayres, T.R.: 1977, A reexamination of solar upper photosphere models, the calcium abundance, and empirical damping parameters. *ApJ* **213**, 296 – 308. doi:10.1086/155156.

Ayres, T.R.: 1989, How deep can one see into the sun? *Sol. Phys.* **124**, 15 – 22. doi:10.1007/BF00146516.

Ayres, T.R., Linsky, J.L.: 1975, Stellar model chromospheres. III - Arcturus /K2 III/. *ApJ* **200**, 660 – 674. doi:10.1086/153835.

Ayres, T.R., Linsky, J.L., Shine, R.A.: 1974, Stellar Model Chromospheres. H. Procyon (F5 Iv/v). *ApJ* **192**, 93 – 110. doi:10.1086/153039.

Barklem, P.S., O'Mara, B.J.: 1998, The broadening of strong lines of Ca+, Mg+ and Ba+ by collisions with neutral hydrogen atoms. *MNRAS* **300**, 863 – 871. doi:10.1046/j.1365-8711.1998.t01-1-01942.x.

Beck, C., Schmidt, W., Rezaei, R., Rammacher, W.: 2008, The signature of chromospheric heating in Ca II H spectra. *A&A* **479**, 213 – 227. doi:10.1051/0004-6361:20078410.

Bellot Rubio, L.R., Ruiz Cobo, B., Collados, M.: 1997, Flux-Tube Model Atmospheres and Stokes V Zero-crossing Wavelengths. *ApJ* **478**, L45. doi:10.1086/310543.

Carlsson, M., Stein, R.F., Nordlund, Å., Scharmer, G.B.: 2004, Observational Manifestations of Solar Magnetoconvection: Center-to-Limb Variation. *ApJ* **610**, 137 – 140. doi:10.1086/423305.

Fontenla, J.M., Balasubramaniam, K.S., Harder, J.: 2007, Semiempirical Models of the Solar Atmosphere. II. The Quiet-Sun Low Chromosphere at Moderate Resolution. *ApJ* **667**, 1243 – 1257. doi:10.1086/520319.

Frutiger, C., Solanki, S.K., Fligge, M., Bruls, J.H.M.J.: 2000, Properties of the solar granulation obtained from the inversion of low spatial resolution spectra. *A&A* **358**, 1109 – 1121.

Gadun, A.S.: 2000, Two-dimensional nonstationary magnetogranulation. *Kinematika i Fizika Nebesnykh Tel* **16**, 99 – 120.

Gadun, A.S., Sheminova, V.A.: 1988, SPANSAT: the Program for LTE Calculations of Absorption Line Profiles in Stellar Atmospheres. In: *Preprint of the Institute for Theoretical Physics of Academy of Sciences of USSR, ITF-88-87, Kiev*, 3 – 37.

Gadun, A.S., Solanki, S.K., Sheminova, V.A., Ploner, S.R.O.: 2001, A formation mechanism of magnetic elements in regions of mixed polarity. *Sol. Phys.* **203**, 1 – 7.

Gingerich, O., Noyes, R.W., Kalkofen, W., Cuny, Y.: 1971, The Harvard-Smithsonian reference atmosphere. *Sol. Phys.* **18**, 347 – 365. doi:10.1007/BF00149057.

Gurtovenko, E.A., Sheminova, V.A.: 1986, 'Crossing' method for studying the turbulence in solar and stellar atmospheres. I - Application to the sun. *Sol. Phys.* **106**, 237 – 247. doi:10.1007/BF00158494.

Henriques, V.M.J., Kiselman, D.: 2009, Temperature stratification in the Sun's photosphere in high horizontal resolution using Ca II H filtergrams. *MemSAI* **80**, 639 – 646.

Henriques, V.M.J., Kiselman, D., van Noort, M.: 2010, Photospheric Temperatures from Ca II H. In: S. S. Hasan and R. J. Rutten (ed.) *Magnetic Coupling between the Interior and Atmosphere of the Sun*, 511 – 512. doi:10.1007/978-3-642-02859-5-74.

Kupka, F., Piskunov, N., Ryabchikova, T.A., Stempels, H.C., Weiss, W.W.: 1999, VALD-2: Progress of the Vienna Atomic Line Data Base. *A&A Suppl.* **138**, 119 – 133. doi:10.1051/aas:1999267.

Leenaarts, J., Rutten, R.J., Carlsson, M., Uitenbroek, H.: 2006a, A comparison of solar proxy-magnetometry diagnostics. *A&A* **452**, 15 – 18. doi:10.1051/0004-6361:20065182.

Leenaarts, J., Rutten, R.J., Sütterlin, P., Carlsson, M., Uitenbroek, H.: 2006b, DOT tomography of the solar atmosphere. VI. Magnetic elements as bright points in the blue wing of Hα. *A&A* **449**, 1209 – 1218. doi:10.1051/0004-6361:20054482.

Leenaarts, J., Rutten, R.J., Reardon, K., Carlsson, M., Hansteen, V.: 2010, The Quiet Solar Atmosphere Observed and Simulated in Na I D_1. *ApJ* **709**, 1362 – 1373. doi:10.1088/0004-637X/709/2/1362.

Mihalas, D.: 1967, The calculation of model sttelar atmospheres. In: *Methods in Computational Physics. New York/London. Academic Press.* **7**, 1 – 52.

Neckel, H.: 1999, Announcement Spectral Atlas of Solar Absolute Disk-averaged and Disk-Center Intensity from 3290 to 12510 A (Brault and Neckel, 1987). *Sol. Phys.* **184**, 421 – 421.

Neckel, H., Labs, D.: 1984, The solar radiation between 3300 and 12500 A. *Sol. Phys.* **90**, 205 – 258. doi:10.1007/BF00173953.

Owocki, S.P., Auer, L.H.: 1980, Two-dimensional radiative transfer. II - The wings of CA K and MG K. *ApJ* **241**, 448 – 458. doi:10.1086/158358.

Rouppe van der Voort, L.H.M.: 2002, Penumbral structure and kinematics from high-spatial-resolution observations of Ca II K. *A&A* **389**, 1020 – 1038. doi:10.1051/0004-6361:20020638.

Rutten, R.J.: 1995, Chromospheric Oscillations. In: *Helioseismology*, *ESA Special Publication* **376**, 151 – 163.

Sheminova, V.A., Rutten, R.J., Rouppe van der Voort, L.H.M.: 2005, The wings of Ca II H and K as solar fluxtube diagnostics. *A&A* **437**, 1069 – 1080. doi:10.1051/0004-6361:20042593.

Shine, R.A., Linsky, J.L.: 1974, A facular model based on the wings of the Ca ii lines. *Sol. Phys.* **37**, 145 – 150. doi:10.1007/BF00157850.

Shine, R.A., Milkey, R.W., Mihalas, D.: 1975, Resonance Line Transfer with Partial Redistribution. V. The Solar CA II Lines. *ApJ* **199**, 724 – 733. doi:10.1086/153744.

Solanki, S.K., Brigljevic, V.: 1992, Continuum brightness of solar magnetic elements. *A&A* **262**, 29 – 32.

Spruit, H.C.: 1974, A model of the solar convection zone. *Sol. Phys.* **34**, 277 – 290. doi:10.1007/BF00153665.

Stein, R.F., Nordlund, A.: 1998, Simulations of Solar Granulation. I. General Properties. *ApJ* **499**, 914 – 933. doi:10.1086/305678.

Tritschler, A., Uitenbroek, H.: 2006, The Contrast of Magnetic Flux Concentrations at Near-Infrared and Visible Wavelengths. *ApJ* **648**, 741 – 752. doi:10.1086/505700.

Uitenbroek, H.: 1989, Operator perturbation method for multi-level line transfer with partial redistribution. *A&A* **213**, 360 – 370.

Uitenbroek, H., Criscuoli, S.: 2011, Why One-dimensional Models Fail in the Diagnosis of Average Spectra from Inhomogeneous Stellar Atmospheres. *ApJ* **736**, 69. doi:10.1088/0004-637X/736/1/69.

Uitenbroek, H., Tritschler, A., Rimmele, T.: 2007, The Discrepancy in G-Band Contrast: Where is the Quiet Sun? *ApJ* **668**, 586 – 593. doi:10.1086/521217.

Wedemeyer, S., Freytag, B., Steffen, M., Ludwig, H., Holweger, H.: 2004, Numerical simulation of the three-dimensional structure and dynamics of the non-magnetic solar chromosphere. *A&A* **414**, 1121 – 1137. doi:10.1051/0004-6361:20031682.